ACS NANO
www.acsnano.org
ARTICLE

Experimental Study of the Detection Limit in Dual-Gate Biosensors Using Ultrathin Silicon Transistors

Ting Wu,[†] Abdullah Alharbi,[†] Kai-Dyi You,[†] Kim Kisslinger,[‡] Eric A. Stach,[‡] and Davood Shahrjerdi*,[†]

[†]Department of Electrical and Computer Engineering, New York University, Brooklyn, New York 10003, United States
[‡]Center for Functional Nanomaterials, Brookhaven National Laboratory, Upton, New York 11973, United States

S *Supporting Information*

ABSTRACT: **Dual-gate field-effect biosensors (bioFETs) with asymmetric gate capacitances were shown to surpass the Nernst limit of 59 mV/pH. However, previous studies have conflicting findings on the effect of the capacitive amplification scheme on the sensor detection limit, which is inversely proportional to the signal-to-noise ratio (SNR). Here, we present a systematic experimental investigation of the SNR using ultrathin silicon transistors. Our sensors operate at low voltage and feature asymmetric front and back oxide capacitances with asymmetry factors of 1.4 and 2.3. We demonstrate that in the dual-gate configuration, the response of our bioFETs to the pH change increases proportional to the asymmetry factor and indeed exceeds the Nernst limit. Further, our results reveal that the noise amplitude also increases in proportion to the asymmetry factor. We establish that the commensurate increase of the noise amplitude originates from the intrinsic low-frequency characteristic of the sensor noise, dominated by number fluctuation. These findings suggest that this capacitive signal amplification scheme does not improve the intrinsic detection limit of the dual-gate biosensors.**

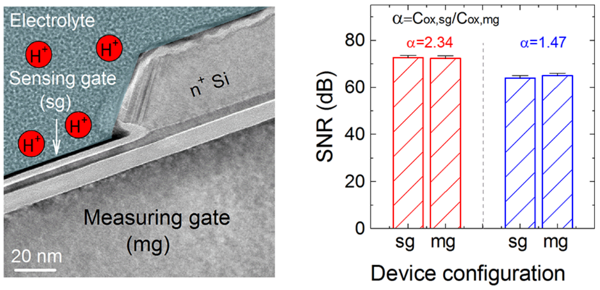

KEYWORDS: *detection limit, biosensor, ultrathin silicon, silicon-on-insulator, bioFETs, super-Nernstian*

Development of new sensing paradigms underpins many exciting discoveries in life sciences. The primary objective of the emergent sensing technologies is often common, which is to enable high-throughput screening of biochemical reactions with enhanced detection accuracy at lower cost. Among various emerging technologies, the pioneering work of Bergveld[1] revealed a new direction for massively parallel detection of biochemical reactions using silicon field-effect transistors (FETs)—the building block of modern integrated circuits. In fact, conventional bulk silicon transistors are now used commercially for biosensing.[2] Further, the evolution of the transistor technology to use nanoscale channel materials will directly benefit biochemical FET sensors (bioFETs) at the fundamental level. Specifically, many studies have demonstrated the improvement of the bioFET sensor response to external charges by increasing the surface-to-volume ratio of the channel material using nanowire,[3,4] nanotube,[5] and nanoribbon[6,7] structures. These bioFETs can detect a variety of biochemical reactions with concentrations below a few picomolars.[3,8,9] However, research is still ongoing to improve the detection limit of bioFETs through materials and device innovations.

In principle, the detection limit of a sensor is inversely proportional to the signal-to-noise ratio (SNR). Boosting the detection accuracy of a sensor, therefore, requires strategies for improving its signal or noise characteristics. One exciting development relates to the amplification of the signal using dual-gate bioFETs through capacitive coupling.[10,11] Several reports have experimentally shown the super-Nernstian characteristic of these bioFETs,[12,13] which is the increase of the sensitivity to the pH change beyond the Nernst limit of 59 mV/pH. However, previous experimental studies of the SNR in relation to the capacitive signal amplification are inconclusive.[14,15] Specifically, it is unclear whether the intrinsic detection limit of the sensor will improve as a result of the signal amplification. The answer to this question is the subject of this work.

Here, we use ultrathin silicon biosensors with asymmetric front and back capacitances as the model system to draw insight into the intrinsic characteristics of bioFETs in the single- and the dual-gate configurations. Our bioFET fabrication process

Received: May 1, 2017
Accepted: June 21, 2017
Published: June 21, 2017

DOI: 10.1021/acsnano.7b02986
ACS Nano 2017, 11, 7142−7147

leverages the technological advances in nanomanufacturing of high-performance silicon transistors. This is to minimize the adverse effects of nonidealities such as charge trapping and high contact resistance, which might otherwise distort the intrinsic signal and noise characteristics of the sensor. We first show the super-Nernstian characteristic of our bioFETs and then demonstrate that the inherent low-frequency noise of the sensor negates the capacitive signal amplification. Together, our findings indicate that the intrinsic detection limit of the super-Nersntian dual-gate bioFETs is comparable with the single-gate biosensors.

Low-Voltage bioFETs with Sub-10 nm Thin Silicon. Our dual-gate bioFETs were fabricated from custom-made silicon-on-insulator (SOI) wafers that feature ultrathin silicon (50−70 Å), sub-10 nm buried oxide (BOX), and p^+ silicon handle substrates. We describe the fabrication process of our custom-made SOI wafers in the Supporting Information. Previous reports on dual-gate silicon bioFETs[7,12,15] used conventional SOI wafers, which have a thick BOX layer (at least 10 times thicker than that of our SOI) and a low-doped silicon handle substrate. The BOX and the handle substrate constitute the back gate in these transistors. The thick BOX layer, however, increased the operating voltage of those bioFETs. Furthermore, the voltage dependence of the partially depleted low-doped silicon underneath the BOX leads to uncertainty in evaluating the back-gate capacitance. Accurate estimation of this capacitance is particularly important for evaluating the signal and the noise characteristics of the device. Our custom-made SOI wafers overcome these issues.

Figure 1a schematically depicts the cross-sectional structure of our device. The transistor channel is undoped, while thermal SiO_2 films passivate the front and back surfaces of the silicon channel, resulting in a low density of localized gap states at these interfaces. We used HfO_2 as the sensing surface due to its superior protonation affinity compared with SiO_2. To minimize the effect of the parasitic access resistance, we used an implant-free process, featuring highly doped n^+ epitaxial raised source and drain regions.[16] Finally, a low-temperature nickel silicide process was performed at 420 °C to define the source and drain contact pads. The transmission electron microscopy (TEM) images in Figure 1b,c illustrate the structural details of two bioFETs with different front and back oxide capacitances.

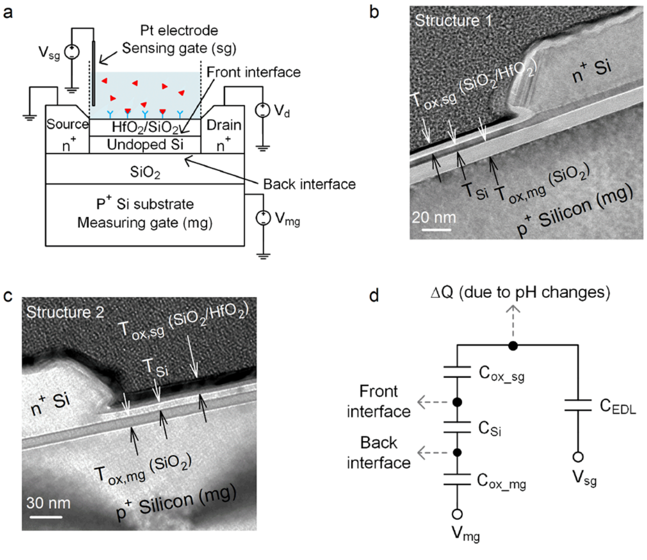

Figure 1. Ultrathin dual-gate silicon bioFETs. (a) Schematic illustration of a dual-gate bioFET. The front channel is solution-gated and the bottom channel is biased by a p^+ global back gate. (b and c) Cross-sectional TEM images of two bioFETs with asymmetric front and back oxide capacitances. (d) Electrical model of the dual-gate bioFET.

RESULTS AND DISCUSSION

In super-Nernstian dual-gate bioFETs, the top channel is solution-gated (sensing gate, sg) and the pH change occurs on the surface of the front oxide. The sensor response is measured by the back gate (measuring gate, mg), biased in strong inversion. The inversion charges capacitively follow the change of pH according to the electrical model in Figure 1d. In this model, $C_{ox,sg}$, $C_{ox,mg}$, C_{Si}, and C_{EDL} are the area-normalized capacitances associated with the front oxide, the bottom oxide, the silicon depletion region, and the electrical double layer. An ionic electrolyte with sufficiently high concentration yields a relatively large C_{EDL}.[17] Therefore, the effect of this capacitance can be ignored in the model. Now consider a case where the front channel is depleted and the pH of the solution changes by ΔpH. Assuming a constant-current mode measurement, the ratio of V_{th} shift measured by the back measuring gate to that measured by the top sensing gate is given by the following expression:[18]

$$\frac{\Delta V_{th,mg}}{\Delta V_{th,sg}}\Big|_{\Delta pH} = \frac{C_{ox,sg}\cdot(C_{Si} + C_{it,sg})}{C_{ox,mg}\cdot(C_{ox,sg} + C_{Si} + C_{it,sg})} \tag{1}$$

where $C_{it,sg}$ is the area-normalized capacitance associated with the trap states at the front interface. For a transistor with ultrathin silicon channel (*i.e.*, $C_{Si} \gg C_{ox}$) and low D_{it}, this expression is reduced to the ratio of the front to back oxide capacitances (*i.e.*, $\approx C_{ox,sg}/C_{ox,mg}$). Furthermore, this result is similar to the case where both front and bottom channels are biased in strong inversion.[12,13] These analytical expressions form the working principle of dual-gate bioFETs for amplifying the sensor response. Therefore, a dual-gate bioFET with $C_{ox,sg} > C_{ox,mg}$ can amplify the sensor response in proportion to this capacitance ratio. We refer to this ratio as the asymmetry factor α.

Electrical Characterization of bioFETs. We now proceed to describe the electrical measurements of our bioFETs. A fluidic chamber was mounted on each sample, and a platinum (Pt) wire was used for applying voltage to the electrolyte. In our experiments, we used standard 1× phosphate-buffered saline (PBS) solution (see Methods). The transfer characteristics of our transistors are free from hysteresis, and the gate leakage current is small (see Supporting Information). To quantify α, we measured the transfer characteristics of the transistors as a function of the back-gate voltage (V_{mg}) at different top-gate voltages (V_{sg}), as shown in Figure 2a,b. The threshold voltage ($V_{th,mg}$) was then extracted and plotted *versus* V_{sg} (Figure 2c). The slope of the fitted line in this plot gives α of about 2.34 and 1.47 for structures 1 and 2, respectively. The results also suggest that our bioFETs can amplify the signal according to the ratio $C_{ox,sg}/C_{ox,mg}$ for a wide range of V_{sg}, where the biasing condition of the front channel spans from depletion to inversion. In previous reports, this maximum amplification level was achieved only when the front and the bottom channels were simultaneously biased in inversion.[12,19] Alternatively, α can be found from the transconductance (g_m) characteristics of the transistors (see Supporting Information).

DOI: 10.1021/acsnano.7b02986
ACS Nano 2017, 11, 7142−7147

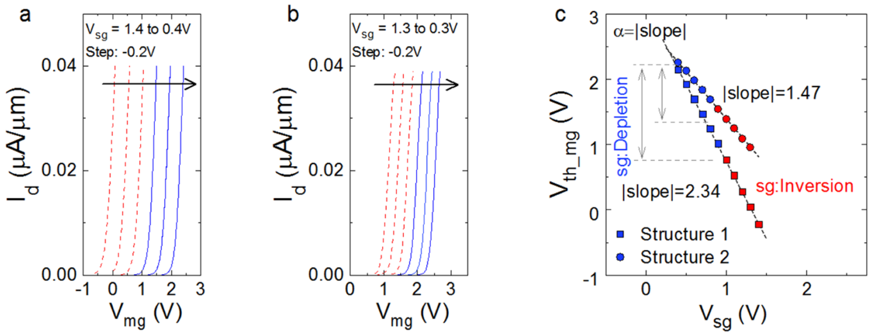

Figure 2. Estimation of the asymmetry factor. Corresponding transfer characteristics of (a) structure 1 and (b) structure 2, as a function of the back-gate voltage (V_{mg}) at different V_{sg}. The blue and red curves represent the biasing conditions at which the front channel is in depletion and inversion, respectively. (c) The slope of the fitted line gives α of 2.34 and 1.47 for the structures 1 and 2, respectively.

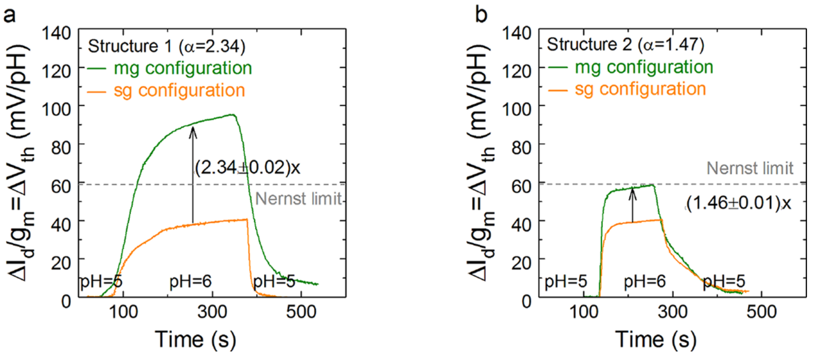

Figure 3. pH Sensing experiments. Typical response of dual-gate bioFETs with α of (a) 2.34, and (b) 1.47, measured in the sg and the mg configurations. The change of the drain current was continuously monitored while flowing PBS with different pH values. The amplitude of the signal increased by a factor of α when measuring the sensor response using the back gate.

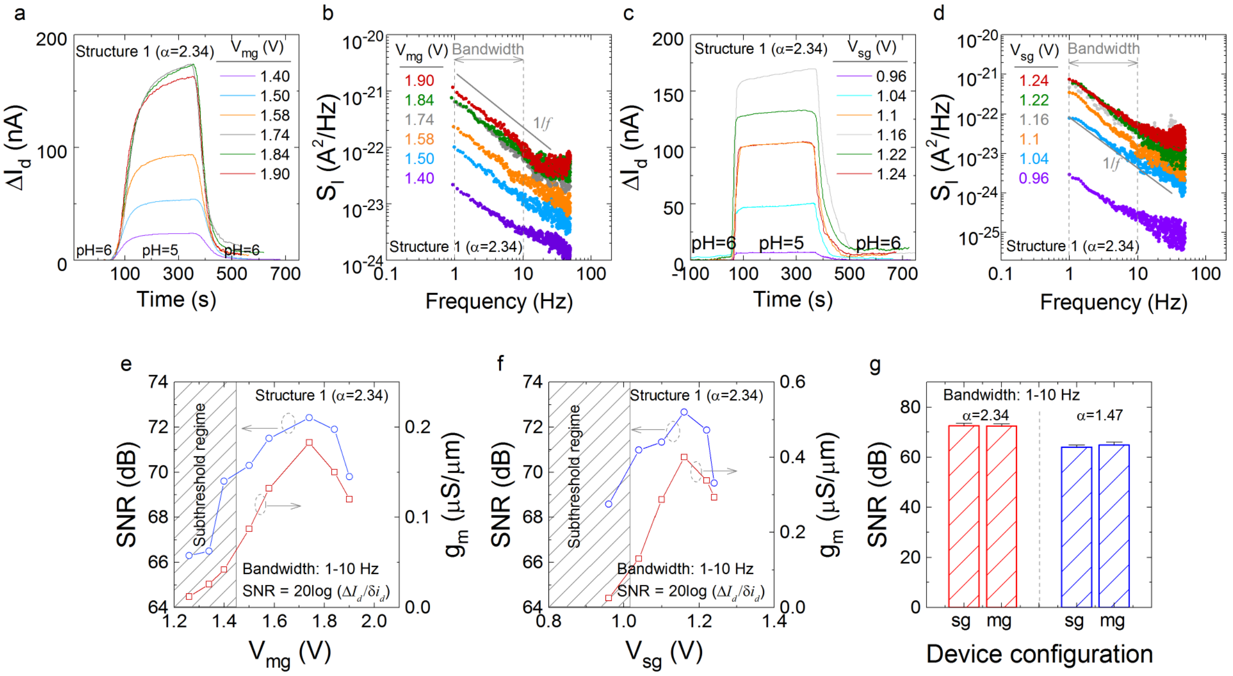

Figure 4. Optimal operating regime of a dual-gate bioFET. (a) pH sensing in the mg configuration as a function of the back gate bias V_{mg}. (b) Corresponding power spectral density of the current noise, measured at different V_{mg}. (c and d) Similar experiments were performed in the sg configuration. (e and f) SNR is maximum in the linear regime at about the peak transconductance for both the sg and mg configurations. (g) Comparison of the maximum SNR, measured in the sg and the mg configurations, for structures 1 and 2. Despite the apparent amplification of the ΔV_{th} in the mg configuration, as shown in Figure 3, the maximum SNR remains unchanged.

DOI: 10.1021/acsnano.7b02986
ACS Nano 2017, 11, 7142−7147

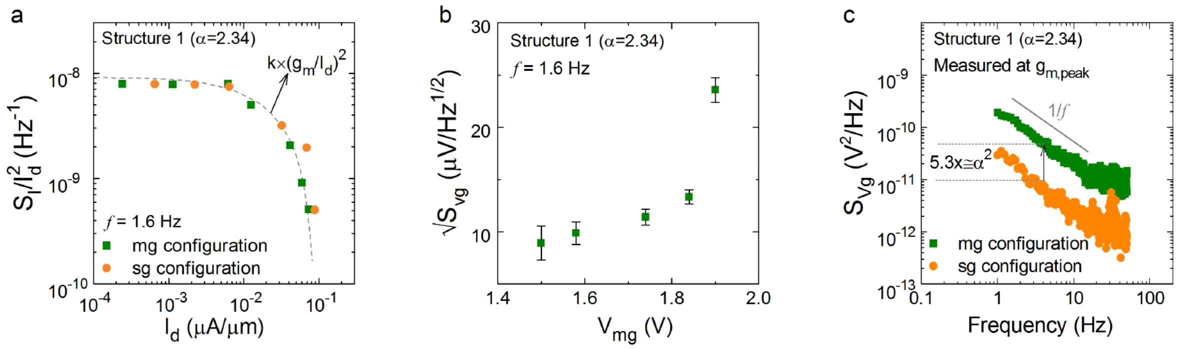

Figure 5. Typical noise characteristics of a dual-gate bioFET. (a) Normalized current noise power was measured in the sg and the mg configurations. The number fluctuation model can explain the noise behavior, confirmed by the $k \times (g_m/I_d)^2$ fit to the data. (b) The weak dependence of the gate voltage noise to V_{mg} in the linear regime also indicates the dominance of the number fluctuation. (c) Comparison of the voltage noise power density in the mg and the sg configurations. The ratio of the noise power density is equal to α^2, because $S_{Vg} \approx S_{VFB}$ (see eqs 2 and 3.).

The extracted values for α using the electrical measurements agree with those estimated from the cross-sectional TEM images by using $\alpha = T_{ox,mg}/T_{ox,sg}$, where $T_{ox,sg}$ and $T_{ox,mg}$ are the equivalent oxide thickness of the sensing and the measuring oxides, respectively.

pH Sensing Experiments. The pH sensing is commonly used in the literature as the standard method for benchmarking the sensitivity of bioFETs. To examine the amplification properties of our bioFETs, we performed pH sensing experiments. For each bioFET, we first measured the sensor response by the top gate (sensing gate), while the bottom channel was biased in depletion. Then, we repeat the sensing experiment while measuring the sensor response using the back gate (measuring gate) and biasing the front channel in depletion. The first experiment represents the sensing properties of a single-gate nanoribbon transistor, while the second measurement illustrates the sensing response of a dual-gate bioFET. We denote these two sensing experiments as the sg and the mg configurations, respectively. In Figure 3a, we plot the temporal sensor response (ΔV_{th}) due to the change of pH, in the sg and the mg configurations. Since the sensors operate in the linear regime (V_{ds} = 100 mV), we calculated ΔV_{th} from $\Delta I_d/g_m$.[20] From the data, we observed that the sensor response in the mg configuration indeed exceeds the Nernst limit. Furthermore, the ratio of $\Delta V_{th,mg}$ to $\Delta V_{th,sg}$ corresponds to the asymmetry factors of our bioFETs, confirming the amplification of the sensor response through capacitive coupling.

Limit of Detection. The detection limit of a sensor is inversely proportional to its maximum SNR. It is, therefore, important to first identify the optimal operating region at which SNR is maximum. This topic has been the subject of extensive research. Previous studies have established that the sensitivity of a bioFET (when defined as $\Delta I_d/I_d$) is always maximum in the subthreshold regime, because of the exponential dependence of the current on the gate voltage. However, the reports on the optimal operating region have been inconsistent. Some reports indicate that the maximum SNR occurs at the subthreshold regime,[15,21,22] while a report by Rajan *et al.* on silicon nanowire bioFETs shows that the SNR reaches its peak value in the linear regime near the peak transconductance, $g_{m,peak}$.[23] The discrepancy is possibly caused by the high contact resistance of FETs or excessive carrier scattering in the channel, which would increase the noise level in the linear region.[24] Despite many reports for single-gate bioFETs, such study is still missing for dual-gate bioFETs. Therefore, we measured the signal (ΔI_d) and the power spectral density of the current noise (S_I) for a dual-gate sensor with α of 2.3 in the sg and the mg configurations. Figure 4a,b illustrates the corresponding signal and noise characteristics of the bioFET in the mg configuration. The corresponding signal and noise characteristics of the sg configuration are shown in Figure 4c,d. We then obtained SNR from the ratio of $\Delta I_d/\delta i_d$, where δi_d is the root-mean-square (rms) current noise amplitude and is given by $\delta i_d = \sqrt{\int_{BW} S_I df}$. In this expression, BW denotes the measurement bandwidth. To compute and then compare the SNR in the sg and the mg configurations, we assumed a bandwidth of 9 Hz with the lower and the upper frequencies of 1 and 10 Hz. In Figure 4e,f, we plot the measured SNR and the corresponding g_m in the mg and the sg configurations, respectively. Two key observations are made from these plots. First, our results indicate that the maximum SNR for both configurations occurs in the linear regime near the $g_{m,peak}$. This finding is consistent with the report by Rajan *et al.* for single-gate nanowire bioFETs.[23] Second, the sg and the mg configurations give comparable SNR values at their corresponding regions of operation. The summary of the maximum SNR for our bioFETs with α of 2.3 and 1.4 at about their corresponding $g_{m,peak}$ is shown in Figure 4g. From these experiments, we conclude that nanoribbon bioFETs in the single-gate and the dual-gate configurations have similar *intrinsic* detection limits. This finding agrees with the theoretical prediction by Go *et al.*[19]

Noise Characteristics of bioFETs. To understand the physical origin of the unchanged intrinsic detection limit of a dual-gate bioFET, despite the capacitive amplification of the signal, we closely examined the noise characteristics of the sensor with α of 2.3. The intrinsic low-frequency noise of bioFETs is typically dominated by the flicker noise.[25] In fact, the normalized current noise power (S_I/I_d^2) together with the correlated number and mobility fluctuation model[26] can give important information about the origin of the low-frequency noise. The intrinsic S_I/I_d^2 of an FET is given by

$$\frac{S_I}{I_d^2} = \frac{g_m^2 S_{Vg}}{I_d^2} = \frac{g_m^2}{I_d^2}(1 + \beta\mu_n C_{ox}(V_{gs} - V_{th}))^2 S_{VFB} \tag{2}$$

In this equation, S_I and S_{Vg} represent the power spectral density of the drain current noise and the gate voltage noise, which are related by $S_I = g_m^2 S_{Vg}$. S_{VFB} is the power spectral density of the voltage noise at about the flatband. For a well-behaved FET, $S_I/$

DOI: 10.1021/acsnano.7b02986
ACS Nano 2017, 11, 7142−7147

I_d^2 is dominated by the number fluctuation in the subthreshold regime and is almost independent of the gate voltage. However, it begins to decrease rapidly in the linear regime with increasing the inversion charge density. The rate of the decline in the linear regime depends on the mobility fluctuation term in eq 2, in which β is the Coulomb scattering coefficient. Figure 5a shows the typical S_I/I_d^2 characteristics of a dual-gate bioFET, plotted as a function of I_d for both the sg and the mg configurations. The function $k \times (g_m/I_d)^2$ provides a reasonable fit to the data, indicating that that the flicker noise in our bioFETs is dominated by the number fluctuation due to charge trapping. The proportionality constant k represents S_{VFB}. From the fit, we extract $S_{\mathrm{VFB,sg}}$ and $S_{\mathrm{VFB,mg}}$ values of about 2.52×10^{-11} and 1.36×10^{-10} V^2/Hz. From the noise data, the density of interface states D_{it} can be estimated using the following expression:[27]

$$S_{\mathrm{VFB}} = \frac{\lambda k_{\mathrm{B}} T q^2 N_{\mathrm{t}}}{fWLC_{\mathrm{ox}}^{\ 2}} \tag{3}$$

where λ, N_t, and q are the tunneling attenuation distance, the total trap density per unit volume, and the elementary charge. For this dual-gate bioFET, we calculated similar D_{it} $(= \lambda N_{\mathrm{t}})$ of about 4×10^{10} eV^{-1}·cm^{-2} for the front and the bottom interfaces, using $W = 15$ μm, $L = 4$ μm, $f = 1.6$ Hz, and $k_{\mathrm{B}}T = 25$ meV. The top and the back oxide capacitances were estimated from the TEM image in Figure 1. The small density of traps indicates the high quality of the front and the bottom interfaces.

The above noise analysis reveals that the S_{VFB} in the mg configuration is higher than that in the sg configuration by a factor of 5.4 (the ratio of the fitted k values). Also, we observed the weak linear dependence of the $\sqrt{S_{V_g}}$ data on the gate voltage, shown in Figure 5b, indicating that the mobility fluctuation term is negligible (*i.e.*, small β). Hence, the S_{V_g} in the linear regime is almost equal to the S_{VFB}, suggesting that the ratio of the S_{V_g} in the sg and the mg configurations should be similar to the calculated ratio for the k parameters. Indeed, we found out that the ratio of the measured S_{V_g} for both the sg and the mg configurations at about their corresponding $g_{m,\mathrm{peak}}$ is close to the ratio of k parameters, as shown in Figure 5c. In fact, this ratio is equal to α^2. The root square of S_{V_g} integrated over the bandwidth represents the rms voltage noise δV. Using this procedure, we calculated a ratio of about 2.3 for the rms voltage noise in the mg and the sg configurations at about their $g_{m,\mathrm{peak}}$, *i.e.*, $\delta V_{\mathrm{mg}}/\delta V_{\mathrm{sg}}$. On the other hand, we showed earlier that the ratio of the signals of interest measured at about their $g_{m,\mathrm{peak}}$, *i.e.*, $\Delta V_{\mathrm{th,mg}}/\Delta V_{\mathrm{th,sg}}$, is also equal to the α. As a result, the maximum SNRs in the mg and the sg configurations are expected to be comparable, as shown in Figure 4. This finding indicates that the capacitive signal amplification by a dual-gate bioFET does not translate into a commensurate increase of the intrinsic detection limit.

CONCLUSIONS

We fabricated low-voltage dual-gate bioFETs with ultrathin silicon channel and asymmetric front and back oxide capacitances. By engineering the ratio of the front capacitance to the back capacitance, asymmetry factor, our dual-gate bioFETs demonstrated the super-Nernstian characteristics. In our bioFETs, the maximum SNR occurs in the linear regime at about the peak transconductance. We found out that the noise amplitude of a dual-gate bioFET also increases in proportion to the asymmetry factor, thereby negating the capacitive signal amplification. The number fluctuation model can explain the noise characteristics of the sensors. Our work demonstrates experimentally that the SNR, and hence the intrinsic detection limit, of ultrathin silicon bioFETs in the single- and the dual-gate configurations are comparable. The finding of our study can be extended to other dual-gate bioFETs, for which their channel thickness is less than the Debye screening length of the channel material.

METHODS

The 1× PBS solution with pH of 7.4 was prepared using the recipe from Cold Spring Harbor Protocols in distilled deionized water (137 mM NaCl, 2.7 mM KCl, 10 mM Na_2HPO_4, 1.8 mM KH_2PO_4). For the sensing experiments, the pH of the PBS solutions was adjusted by adding diluted HCl to the original 1× PBS solution. The pH values were then verified using a pH meter (OMEGA PHH222). The pH solution was introduced into the fluidic chamber using a custom-made delivery system at 0.8 mL/min.

Temporal responses of the sensors and their corresponding transfer characteristics were measured by Keithley 4200-SCS semiconductor analyzer. The noise measurements were performed using an NI data acquisition card, a low-noise pre-amplifier (SR570), and a spectrum analyzer. The data analysis was then done in MATLAB.

ASSOCIATED CONTENT

Ⓢ Supporting Information

The Supporting Information is available free of charge on the ACS Publications website at DOI: 10.1021/acsnano.7b02986.

> Details of the fabrication process for the custom-made SOI wafers, high magnification TEM images of our bioFETs with different asymmetry factors, the transfer characteristics and the hysteresis of the transfer curves, the transconductance characteristics for both structure 1 and structure 2, as well as voltage noise power density in the mg and the sg configurations for structure 2 (PDF)

AUTHOR INFORMATION

Corresponding Author

*E-mail: davood@nyu.edu.

ORCID

Eric A. Stach: 0000-0002-3366-2153

Davood Shahrjerdi: 0000-0002-5955-1830

Notes

The authors declare no competing financial interest.

ACKNOWLEDGMENTS

This research used resources of the Center for Functional Nanomaterials, which is a U.S. DOE Office of Science Facility, at Brookhaven National Laboratory under contract no. DE-SC0012704. The authors acknowledge Cristina Lubguban for helping with the fabrication of the custom-made SOI substrates.

REFERENCES

(1) Bergveld, P. Development of an Ion-Sensitive Solid-State Device for Neurophysiological Measurements. *IEEE Trans. Biomed. Eng.* **1970**, *BME-17*, 70−71.

(2) Rothberg, J. M.; Hinz, W.; Rearick, T. M.; Schultz, J.; Mileski, W.; Davey, M.; Leamon, J. H.; Johnson, K.; Milgrew, M. J.; Edwards, M.; Hoon, J.; Simons, J. F.; Marran, D.; Myers, J. W.; Davidson, J. F.; Branting, A.; Nobile, J. R.; Puc, B. P.; Light, D.; Clark, T. A.; et al. An Integrated Semiconductor Device Enabling Non-Optical Genome Sequencing. *Nature* **2011**, *475*, 348−352.

(3) Stern, E.; Klemic, J. F.; Routenberg, D. A.; Wyrembak, P. N.; Turner-Evans, D. B.; Hamilton, A. D.; LaVan, D. A.; Fahmy, T. M.; Reed, M. A. Label-Free Immunodetection with CMOS-Compatible Semiconducting Nanowires. *Nature* **2007**, *445*, 519−522.

(4) Elfström, N.; Juhasz, R.; Sychugov, I.; Engfeldt, T.; Karlström, A. E.; Linnros, J. Surface Charge Sensitivity of Silicon Nanowires: Size Dependence. *Nano Lett.* **2007**, *7*, 2608−2612.

(5) Someya, T.; Small, J.; Kim, P.; Nuckolls, C.; Yardley, J. T. Alcohol Vapor Sensors Based on Single-Walled Carbon Nanotube Field Effect Transistors. *Nano Lett.* **2003**, *3*, 877−881.

(6) Elfström, N.; Karlström, A. E.; Linnros, J. Silicon nanoribbons for electrical detection of biomolecules. *Nano Lett.* **2008**, *8*, 945−949.

(7) Fahad, H. M.; Shiraki, H.; Amani, M.; Zhang, C.; Hebbar, V. S.; Gao, W.; Ota, H.; Hettick, M.; Kiriya, D.; Chen, Y.-Z.; Chueh, Y.-L.; Javey, A. Room temperature multiplexed gas sensing using chemical-sensitive 3.5-nm-thin silicon transistors. *Sci. Adv.* **2017**, *3*, e1602557.

(8) Cui, Y.; Lieber, C. M. Functional Nanoscale Electronic Devices Assembled using Silicon Nanowire Building Blocks. *Science* **2001**, *291*, 851−853.

(9) Zheng, G.; Patolsky, F.; Cui, Y.; Wang, W. U.; Lieber, C. M. Multiplexed Electrical Detection of Cancer Markers with Nanowire Sensor Arrays. *Nat. Biotechnol.* **2005**, *23*, 1294−1301.

(10) Spijkman, M.-J.; Brondijk, J. J.; Geuns, T. C.; Smits, E. C.; Cramer, T.; Zerbetto, F.; Stoliar, P.; Biscarini, F.; Blom, P. W.; de Leeuw, D. M. Dual-Gate Organic Field-Effect Transistors as Potentiometric Sensors in Aqueous Solution. *Adv. Funct. Mater.* **2010**, *20*, 898−905.

(11) Lee, I.-K.; Jeun, M.; Jang, H.-J.; Cho, W.-J.; Lee, K. A Self-Amplified Transistor Immunosensor Under Dual Gate Operation: Highly Sensitive Detection of Hepatitis B Surface Antigen. *Nanoscale* **2015**, *7*, 16789−16797.

(12) Knopfmacher, O.; Tarasov, A.; Fu, W.; Wipf, M.; Niesen, B.; Calame, M.; Schonenberger, C. Nernst Limit in Dual-Gated Si-Nanowire FET Sensors. *Nano Lett.* **2010**, *10*, 2268−2274.

(13) Jang, H.-J.; Cho, W.-J. Performance Enhancement of Capacitive-Coupling Dual-Gate Ion-Sensitive field-effect transistor in ultra-thin-body. *Sci. Rep.* **2015**, *4*, 5284.

(14) Huang, Y.-J.; Lin, C.-C.; Huang, J.-C.; Hsieh, C.-H.; Wen, C.-H.; Chen, T.-T.; Jeng, L.-S.; Yang, C.-K.; Yang, J.-H.; Tsui, F.; Liu, Y.-S.; Chen, M. High Performance Dual-Gate ISFET with Non-Ideal Effect Reduction Schemes in a SOI-CMOS Bioelectrical SoC. Proceedings from the *IEEE International Electron Devices Meeting (IEDM)*, Washington, DC, December 7−9, 2015; IEEE: Piscataway, NJ, 2015; pp 749−750.

(15) Tarasov, A.; Fu, W.; Knopfmacher, O.; Brunner, J.; Calame, M.; Schönenberger, C. Signal-to-Noise Ratio in Dual-Gated Silicon Nanoribbon Field-Effect Sensors. *Appl. Phys. Lett.* **2011**, *98*, 012114.

(16) Cheng, K.; Khakifirooz, A.; Kulkarni, P.; Ponoth, S.; Kuss, J.; Shahrjerdi, D.; Edge, L.; Kimball, A.; Kanakasabapathy, S.; Xiu, K.; Schmitz, S.; Reznicek, A.; Adam, T.; He, H.; Loubet, N.; Holmes, S.; Mehta, S.; Yang, D.; Upham, A.; Seo, S. et al. Extremely Thin SOI (ETSOI) CMOS with Record Low Variability for Low Power System-on-Chip Applications. Proceedings from the *IEEE International Electron Devices Meeting (IEDM)*, December 15−17, 2009, Washington, DC, 2009; IEEE: Piscataway, NJ; pp 1−4.

(17) Stern, E.; Wagner, R.; Sigworth, F. J.; Breaker, R.; Fahmy, T. M.; Reed, M. A. Importance of the Debye Screening Length on Nanowire Field Effect Transistor Sensors. *Nano Lett.* **2007**, *7*, 3405.

(18) Pei, G.; Kan, E.-C. Independently Driven DG MOSFETs for Mixed-Signal Circuits: Part I-Quasi-Static and Nonquasi-Static Channel Coupling. *IEEE Trans. Electron Devices* **2004**, *51*, 2086−2093.

(19) Go, J.; Nair, P. R.; Alam, M. A. Theory of Signal and Noise in Double-Gated Nanoscale Electronic pH Sensors. *J. Appl. Phys.* **2012**, *112*, 034516.

(20) Abe, M.; Murata, K.; Kojima, A.; Ifuku, Y.; Shimizu, M.; Ataka, T.; Matsumoto, K. Quantitative Detection of Protein using a Top-Gate Carbon Nanotube Field Effect Transistor. *J. Phys. Chem. C* **2007**, *111*, 8667−8670.

(21) Gao, X. P.; Zheng, G.; Lieber, C. M. Subthreshold Regime Has the Optimal Sensitivity for Nanowire FET Biosensors. *Nano Lett.* **2010**, *10*, 547.

(22) Heller, I.; Mannik, J.; Lemay, S. G.; Dekker, C. Optimizing the Signal-to-Noise Ratio for Biosensing with Carbon Nanotube Transistors. *Nano Lett.* **2009**, *9*, 377−382.

(23) Rajan, N. K.; Routenberg, D. A.; Reed, M. A. Optimal Signal-to-Noise Ratio for Silicon Nanowire Biochemical Sensors. *Appl. Phys. Lett.* **2011**, *98*, 264107.

(24) Renteria, J.; Samnakay, R.; Rumyantsev, S.; Jiang, C.; Goli, P.; Shur, M.; Balandin, A. Low-Frequency 1/f Noise in MoS2 Transistors: Relative Contributions of the Channel and Contacts. *Appl. Phys. Lett.* **2014**, *104*, 153104.

(25) Rajan, N. K.; Routenberg, D. A.; Chen, J.; Reed, M. A. 1/f Noise of Silicon Nanowire BioFETs. *IEEE Electron Device Lett.* **2010**, *31*, 615−617.

(26) Ghibaudo, G.; Roux, O.; Nguyen-Duc, C.; Balestra, F.; Brini, J. Improved Analysis of Low Frequency Noise in Field-Effect MOS Transistors. *Phys. Status Solidi A* **1991**, *124*, 571−581.

(27) Jayaraman, R.; Sodini, C. G. A 1/f Noise Technique to Extract the Oxide Trap Density Near the Conduction Band Edge of Silicon. *IEEE Trans. Electron Devices* **1989**, *36*, 1773−1782.

DOI: 10.1021/acsnano.7b02986
ACS Nano 2017, 11, 7142−7147